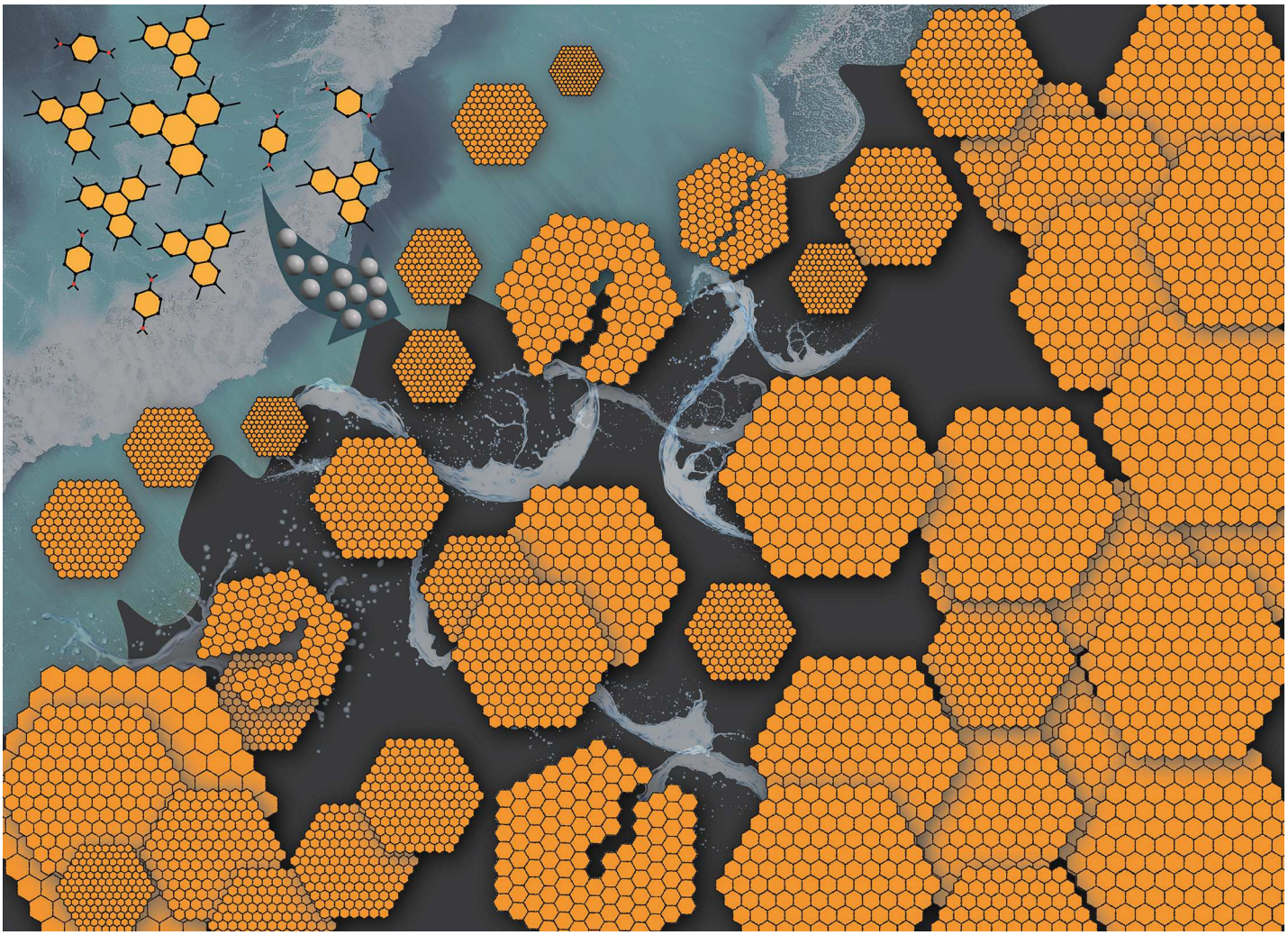

Showcasing research from Professors Meenesh Singh, Anh Ngo, and Santanu Chaudhuri's laboratory, Department of Chemical Engineering, University of Illinois Chicago, Illinois, USA.

Microkinetic insights into the role of catalyst and water activity on the nucleation, growth, and dissolution during COF-5 synthesis

The synthesis pathways for covalent organic frameworks (COFs) involve a complex sequence of reactions over a rippling energy landscape that cannot be described using existing theories. Here, we employ time-resolved *in-situ* FT-IR coupled with a large-scale microkinetic model to reveal previously unrecognized roles of catalyst pKa and water on COF synthesis. COF yield increases with decreasing catalyst pKa, whereas water reduces the growth rate and broadens the size distribution.

As featured in:

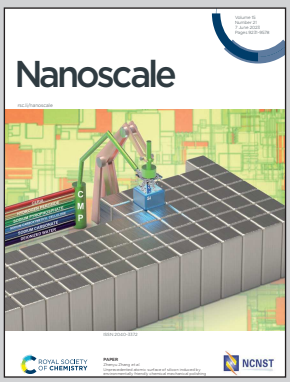

See Meenesh R. Singh *et al.*, *Nanoscale*, 2023, **15**, 9329.

ROYAL SOCIETY OF CHEMISTRY

rsc.li/nanoscale

Registered charity number: 207890

Nanoscale

PAPER

View Article Online
View Journal | View Issue

Cite this: *Nanoscale*, 2023, **15**, 9329

Microkinetic insights into the role of catalyst and water activity on the nucleation, growth, and dissolution during COF-5 synthesis†

Anish V. Dighe, ‡[a] Rajan R. Bhawnani, ‡[a] Prem K.R. Podupu, [a] Naveen K. Dandu,[a,b] Anh T. Ngo,[a,b] Santanu Chaudhuri[a,b] and Meenesh R. Singh *[a]

The chemical pathway for synthesizing covalent organic frameworks (COFs) involves a complex medley of reaction sequences over a rippling energy landscape that cannot be adequately described using existing theories. Even with the development of state-of-the-art experimental and computational tools, identifying primary mechanisms of nucleation and growth of COFs remains elusive. Other than empirically, little is known about how the catalyst composition and water activity affect the kinetics of the reaction pathway. Here, for the first time, we employ time-resolved *in situ* Fourier transform infrared spectroscopy (FT-IR) coupled with a six-parameter microkinetic model consisting of ~10 million reactions and over 20 000 species. The integrated approach elucidates previously unrecognized roles of catalyst pK_a on COF yield and water on growth rate and size distribution. COF crystalline yield increases with decreasing pK_a of the catalysts, whereas the effect of water is to reduce the growth rate of COF and broaden the size distribution. The microkinetic model reproduces the experimental data and quantitatively predicts the role of synthesis conditions such as temperature, catalyst, and precursor concentration on the nucleation and growth rates. Furthermore, the model also validates the second-order reaction mechanism of COF-5 and predicts the activation barriers for classical and non-classical growth of COF-5 crystals. The microkinetic model developed here is generalizable to different COFs and other multicomponent systems.

Received 29th November 2022,
Accepted 7th April 2023

DOI: 10.1039/d2nr06685h

rsc.li/nanoscale

Introduction

Covalent-organic frameworks (COFs) are crystalline materials formed by strong covalent bonds that result in high surface area and porosity, enabling a variety of applications across domains, including gas storage,[1] catalysis,[2] carbon capture,[3] sensing,[4,5] and energy storage.[6] Reagents and process conditions such as solvent or antisolvent compositions, catalyst, pH, temperature, and concentration have all been observed to affect the kinetics of COF reticular synthesis, but their mechanism is not well-discerned.[7]

The formation of COFs, and other framework materials like metal–organic frameworks (MOFs), is often described with the help of secondary building units (SBUs).[7–9] COF SBUs contain two or more organic molecules linked through a metalloid (boron – boronic ester, boroxine groups) or non-metallic linkers (nitrogen – imide/imine groups). In COFs with ester linkages, the bonds are reversible, allowing the deformation of their crystalline framework during synthesis.[10] Furthermore, pH-dependent speciation has also been observed to influence the rate of bond formation,[11–13] which in turn determines the crystallinity of the COF.[14–16] The synthesis pathway and the chemistry of SBU formation that can dictate the dimensionality of the COF frameworks[17] have been studied experimentally and computationally.

Researchers have shown that COFs follow both classical (monomeric attachment) and non-classical (oriented attachment) nucleation and growth.[18–20] Computational approaches such as density functional theory (DFT),[21–23] molecular dynamics (MD),[24] kinetic Monte-Carlo (kMC)[14,15,25] are often used to derive mechanisms of COF synthesis from the study of a subset of reactions involved in SBU formation. It is, therefore, necessary to derive alternative unbiased theoretical-computational models which comprehensively capture the complete pathway of COF synthesis, including (i) speciation of the reactants, (ii) the SBU formation, and (iii) nucleation and growth.

COF synthesis mechanisms have been analyzed and validated using *in situ* X-ray diffraction (XRD)[26–28] – specifically

[a]*Department of Chemical Engineering, University of Illinois at Chicago, Chicago, IL 60607, USA. E-mail: mrsingh@uic.edu; Tel: +1 (312) 996-3424*
[b]*Argonne National Laboratory, Lemont, IL 60439, USA*
†Electronic supplementary information (ESI) available. See DOI: https://doi.org/10.1039/d2nr06685h
‡These authors contributed equally.

small and wide-angle X-ray scattering (SAXS/WAXS) techniques, and also electron microscopy,[29,30] which can yield comprehensive information of their synthesis at much smaller length and time scales.[31,32] However, performing these characterizations across ranges of solvent compositions is time-consuming. *In situ* SAXS/WAXS are elaborate and are less readily available, while electron microscopy can only capture information across time scales for a few COF crystallites. In addition to SAXS, *in situ* near-infrared and nuclear magnetic resonance techniques have been implemented to understand the kinetic effects of various processing conditions on 2D boronate ester COFs.[28,33–35] Studies have been performed to understand the effect of solvents using the mentioned *in situ* techniques, to gain limited mechanistic insights, and hypothesize a possible reaction pathway for a coupled crystallization–polymerization phenomena of COF-5 formation.[33,36] However, the role of additive catalytic species has been largely unexplored, which can provide further insight into the esterification mechanism of COF-5.

Although independent experimental and computational investigations have been conducted previously, very few reports have utilized both experiments and computations to identify a mechanism of COF synthesis. There is a need for a combined experimental and theoretical approach to quantitatively understand the mechanism of COF-5 synthesis and identify key molecular events that govern COF nucleation and growth processes. In this work, a time-dependent synthesis of COF-5 obtained from *in situ* Fourier transform infrared spectroscopy (FT-IR)[37] and *ex situ* powder X-ray diffraction (PXRD) is analyzed using a robust microkinetic model to precisely predict COF yield and grain size distribution. The microkinetic model was developed to include kinetics of SBU formation followed by classical and non-classical aggregation of SBUs to form crystals. The model system chosen here was COF-5, which is a boronate ester that results from the reaction between an acidic precursor (1,4-diboronic acid) and a catechol (hexahydroxytriphenylene (HHTP)). This esterification reaction is reversible due to hydrolysis of SBU in the presence of water (byproduct). To further alter and gain control over the backward reaction for a higher yield of COF, the effect of catalyst speciation is studied. For this purpose, COF-5 was synthesized using catalysts of decreasing pK_a values, namely methanol (pK_a 15.5), phenol (pK_a 10), acetic acid (pK_a 4.74), and formic acid (pK_a 3.75). The microkinetic model was developed to predict the effect of speciation using only the pK_a values of the catalysts in the kinetic expression.[38] Experiments performed at different temperatures allow estimation of the rate constants involved in the synthesis of COF-5. Based on the results, we first show that the initiation reaction of COF-5 proceeds through the acid-catalyzed esterification pathway leading to the formation of SBU and water.[39] The formation of SBU depends on the speciation of the reactants that is govern by the pK_a of the catalyst. Second, we show that higher-order SBUs are formed due to non-classical nucleation pathways, and the yield of COF-5 strongly depends on the rate of formation of SBUs (initiation reaction). Third, we show that the non-classical nucleation mechanism governs the grain size of the COF-5. The high amount of water evolved due to the formation of SBUs then further impedes the formation of larger COF-5 crystals. Overall, the simplicity of coupled theoretical and experimental approaches yields significant insights into COF-5 synthesis, which are usually only possible using elaborate experimental techniques such as *in situ* SAXS/WAXS. The experimental setup and the proposed mechanism of COF-5 formation are shown in Fig. 1.

Materials & methods

Experimental methods

In situ FT-IR and *ex situ* XRD studies were used to measure the yield and crystallinity of COF-5 as a function of different reaction temperatures and catalysts. Briefly, 1 ml of reaction mixture containing 8 mM of HHTP, 12 mM of PBBA, desired catalyst, and solvents (1,4-dioxane and toluene, 4 : 1 v/v mixture) was prepared and analyzed under *in situ* time-resolved FT-IR spectroscopy. The choice of 4 : 1 v/v solvent mixture of dioxane and toluene is used mainly to obtain a homogenous reaction mixture and mediate the diffusion of the dissolved monomers to enhance nucleation of COF-5.[35,40] The batch cell containing the reaction mixture was maintained at desired temperature using a temperature-controlled zinc selenide (ZnSe) crystal plate, and spectra were collected in attenuated total reflectance (ATR) mode. The COF-5 crystals were harvested at various times and analyzed under XRD. Details of the experimental setup and characterizations are included in section S1 of the ESI.†

Computational methods

Based on the insights obtained from the experiments, a detailed reaction schematic was utilized to formulate a six-parameter microkinetic model. The microkinetic model was validated and used to predict the results of COF-5 synthesis at various experimental conditions. The parameters of the precursors were utilized from the experiments, and the SBU structure molecular weight was derived, as shown in section S2 of the ESI.† Density functional theory (DFT) calculations were performed to validate the experimental results further. DFT calculations were performed using Gaussian 16 software package. Details of DFT calculations are provided in section S3 of the ESI.† The details of the theoretical microkinetic model, optimization, and rate calculations are given in sections S4, S5, and S6 of the ESI,† respectively.

Results and discussion

The experimental setup and the characteristic FT-IR spectra of COF-5 are shown in Fig. S1 and S2,† respectively. The molar concentration of COF-5 shown in Fig. S2a† is derived using the known crystal structure of COF-5, and the smallest repeating SBU (SBU_1) found in the crystal structure. Since COF-5 for-

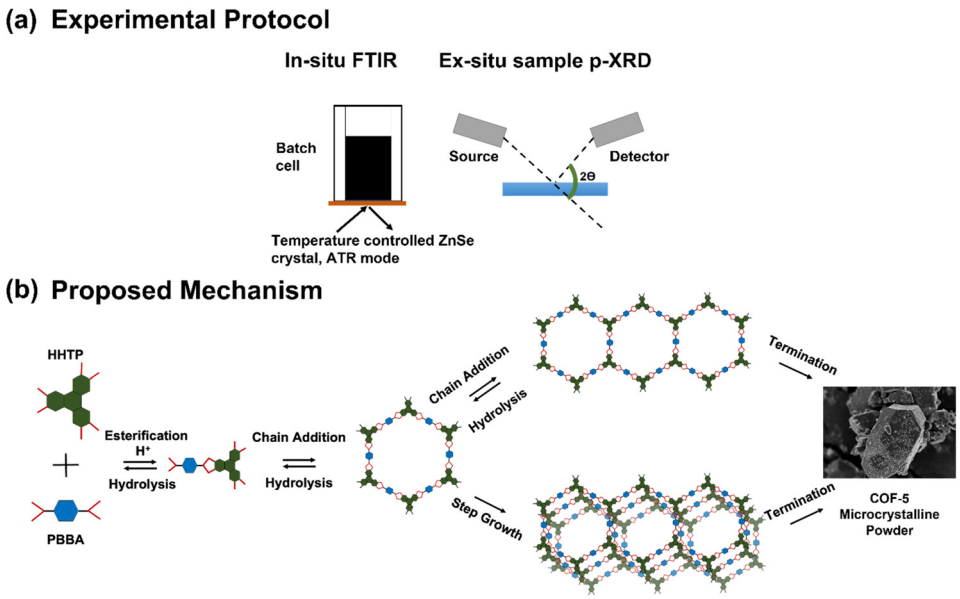

Fig. 1 Overview of the analysis procedure for COF-5 synthesis. (a) The reaction mixture containing reactants hexahydroxytriphenylene (HHTP) and phenylbisboronic acid (PBBA), in a 4 : 1 (v/v) solvent mixture of 1,4-dioxane and toluene with the desired catalyst is added to the batch cell of FT-IR. FT-IR is then operated in attenuated total reflectance (ATR) mode on a temperature-controlled zinc selenide (ZnSe) crystal. The crystals obtained at various time points during the COF-5 formation reaction are collected and analyzed using the *ex situ* PXRD technique. (b) The proposed mechanism of COF-5 is that the reactants HHTP and PBBA form the smallest secondary building unit (SBU_1) of COF-5 and water. SBU_1 undergoes chain addition to form higher-order growth units. Higher-order growth units can result in surface stabilized crystals of COF-5 due to monomer attachment (chain addition) or oriented attachment (step-growth), resulting in the termination phase. Formation of new SBU_1 in the solution or on the surface of the crystal releases water. In turn, water hydrolyzes the boron–oxygen and carbon–oxygen bonds of COF-5 to yield smaller crystals or reactants.

mation is a second order reaction,[35] the molecular structure of SBU_1 can be considered as one part PBBA and one part HHTP with elimination of two water molecules. The molecular weight of SBU_1 is then calculated as 454.04 g mol^{-1}. The concentration of SBU_1 in COF-5 suspension is obtained by dividing the weight of COF-5 by the molecular weight of SBU_1. The formation of SBU_1 results in three strong covalent bonds that are characteristic signatures of COF-5 in the mid-IR region, and those are (i) boron–oxygen (B–O, 1352 cm^{-1} and 1347 cm^{-1}), (ii) carbon–oxygen (C–O, 1241 cm^{-1}), and (iii) boron–carbon (B–C, 1076 cm^{-1}).[39] The intensity of the C–O bond as a function of increasing concentration follows a linear relationship, as shown in the calibration curve in Fig. S3 of the ESI.† The linear relationship and the high confidence (R^2 = 0.996) of fitting of the calibration curve allow estimating the experimental yield of COF-5. Fig. S2b and S2c† show the increase in the intensity of the C–O peak in the experiment carried out at 80 °C with acetic acid and methanol as catalysts, respectively. It is possible that the non-crystalline yield of COF-5 was also captured during the *in situ* measurements since FT-IR is based on bond vibrations. The XRD spectra of the harvested powder of COF-5 confirm its crystallinity.

The difference in the intensity between acetic acid and methanol as catalysts at longer times, as shown in Fig. S2b and S2c,† is mainly due to the change in the buffering capacity of the precursor solution. Fig. 2 quantitatively depicts the

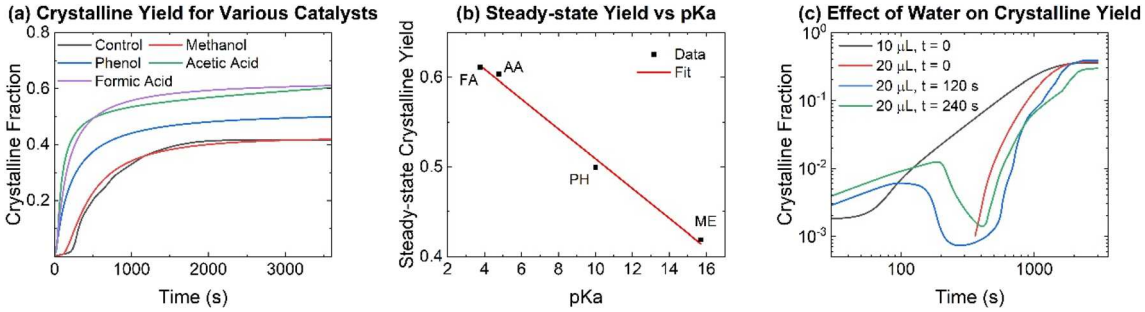

Fig. 2 Effect of catalyst and water on the crystalline yield of COF-5. (a) Experimental crystalline fraction (yield) of COF-5 at various times obtained from *in situ* FTIR as a function of different catalysts in the solution. The solvent condition was maintained at 4 : 1 v/v mixture of dioxane : toluene and T = 80 °C. (b) Relationship between the steady-state yield of COF-5 and the pK_a of the catalysts. (c) Effect of addition of excess water on the crystalline yield of COF-5.

relationship between the solution composition and the crystalline yield. The role of solvents 1,4-dioxane and toluene in the solution is reported in the literature.[35] However, for the first time, we report the role of buffering capacity of the catalyst (additive) and the water dynamics on the crystalline yield. Fig. 2a shows that the crystalline yield increases as the pK_a of the catalyst in the solution decrease. The crystalline yield of COF-5 with no catalyst (control) is the same as the crystalline yield when methanol is used as the catalyst. As pK_a decreases from methanol (pK_a 15.5) to phenol (10) to acetic acid (4.74) and finally to formic acid (3.75), the initial rate of formation of COF-5 and the steady-state crystalline yield increase. The steady-state crystalline yield plotted against pK_a shows a linear relationship (Fig. 2b). This indicates that the rate of the initiation reaction of COF-5 that proceeds through esterification and release of water molecules depends upon the concentration of protons (H^+ ion) in the solution. Two components in the solution affect the total concentration of protons: (i) the catalyst and (ii) the equilibrium dissociation of water into a proton and hydroxyl (OH^-) ions. The pK_a of water dissociation is calculated at various temperatures, and for the temperatures considered in this study, the pK_a varies between 12 and 13.[41] Hence, the dissociation of water is the only dominant proton source in the solution when methanol is used as the catalyst since all the other catalysts have significantly higher pK_a values. The linear relationship further indicates an upper limit for the proton concentration that catalyzes the initiation reaction. Identifying such a limiting rate constant of the initiation reaction would help design the reaction conditions that yield a higher crystalline yield of COF-5.

The effect of buffering capacity is further validated with the help of DFT calculations. The results of these calculations are shown in Fig. S4, S5, and Tables S1, S2 of the ESI.† DFT calculations were performed to understand and quantify the energy change during the intrinsic reaction coordinate of the initiation reaction (HHTP + PBBA). The results show that the activation barrier is highest when the initiation reaction occurs independently (without a catalyst). However, when different catalysts are placed in the vicinity of reactant molecules, the activation barrier decreases. DFT results do not strictly follow the pK_a-dependent trend, as shown in Fig. 2. The mismatch can be attributed to the fewer molecules and steric hindrance effects captured due to molecules' placement in the simulation box. However, lowering of activation barrier in the presence of different additives validates that COF-5 formation proceeds through the acid-catalyzed Fischer esterification process.

Apart from contributing to the net proton concentration of the solution, water molecules can also further hydrolyze the newly formed bonds in the COF-5 reaction. Water was added at different times to understand the crystalline yield to test the hypothesis, and the results are shown in Fig. 2c. 10 μL and 20 μL water were added at the start of the COF-5 synthesis and after 2 and 4 minutes of reaction in separate experiments. When a higher concentration of water is added at the initial time, it significantly increases the lag period resulting in the sigmoidal feature of the crystalline fraction curve. When water is added after 2 or 4 minutes, an immediate reduction in the crystalline fraction is seen, indicating that water hydrolyzes the bonds in COF-5. The steady-state yields of COF-5 in different experimental conditions in Fig. 2c are not the same indicating that water has not fully evaporated from the reaction mixture. If the water had fully evaporated, then according to Le Chatelier's principle, all experimental conditions should have yielded the same steady-state. The experimental results described in Fig. 2 form the basis of the microkinetic model developed for COF-5 synthesis.

The mechanistic insight into the dependence of COF-5 crystalline fraction on reaction conditions is obtained using the microkinetic model, which has been previously benchmarked for MOFs.[38,42] The microkinetic model developed in this study includes (i) acid-catalyzed formation of SBU_1 (initiation), (ii) formation of COF-5 crystals (onset of termination) due to monomer addition (chain addition) and oriented attachment (step growth), and (iii) dissolution (hydrolysis) of the crystals to yield smaller crystals or reactants. The reaction network resulting due to the consideration of all of the processes described above has over 20 000 nodes and 10 million edges. Eight different synthesis conditions corresponding to temperatures – 80 °C, 85 °C, and 90 °C, and catalysts – acetic acid (all listed temperatures), methanol (all listed temperatures), phenol, and formic acid (80 °C) were studied using the microkinetic model. Fig. 3 shows the theoretical (solid black line) and experimental (solid red line) crystal volume fraction with estimated contribution from nucleation (black dashed line). The average standard deviation for experimental data points is reported in Table S3 of the ESI.† The relative contributions of reactions towards the increase in crystal volume fraction are represented as – SBU_1 formation (initiation reaction, blue region), monomer addition (chain addition, green region), oriented attachment resulting in active SBU clusters (step-growth, orange region), and oriented attachment resulting in inactive SBU clusters (termination phase, red region). The parameters required to obtain results from the theoretical model are error minimized using the experimental results depicted in Fig. 3a, b, d, and e. Theoretical results shown in Fig. 3c, and f are predicted using the optimized parameters. Tables S3 and S4 of the ESI† give the information about the experimental data sets used for optimization and the values of the parameters, respectively. Fig. S6–S10† show the error minimized values in the parameter scan.

Relative rate contributions from the theoretical model highlight the effect of pK_a on forming SBU_1. Lower pK_a of acetic acid yields a higher concentration of protons in the solution, allowing faster SBU_1 formation. In other words, a higher rate of initiation in the presence of acetic acid allows the reaction to proceed quickly to the monomer addition and oriented attachment stage. In the case of methanol catalyst, a lower rate of initiation holds the reaction in the SBU_1 formation and monomer addition phase, thus slowing down the transition to the oriented attachment stage. Although the monomer addition phase dictates the crystalline fraction observed in the

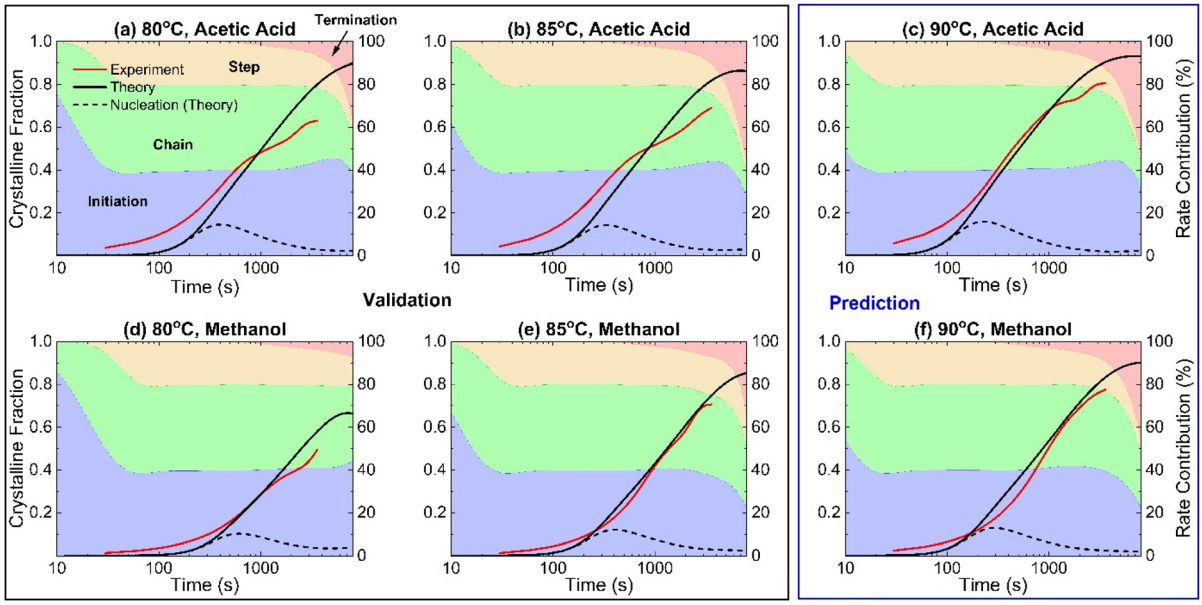

Fig. 3 Mechanistic insights into the yield of COF-5 using coupled theoretical and experimental approaches. In all the panels, the solid red line represents experimental data from *in situ* FTIR experiments, the solid black line represents theoretical crystalline fraction (yield), and the black dashed line represents the theoretical contribution of nuclei towards crystalline fraction. The left *y*-axis represents the crystalline fraction. The background in all the panels represents the relative contribution of initiation reaction (blue), chain addition (green), step-growth (orange), and termination phase (red). The relative rate contribution is represented on the right *y*-axis. The figure title represents the temperature and the catalyst used in the experiments. (a) 80 °C, acetic acid, (b) 85 °C, acetic acid, (c) 90 °C, acetic acid, (d) 80 °C, methanol, (e) 85 °C, methanol, (f) 90 °C, methanol. Legend and terminologies defined in (a) apply to all the panels. Panels enclosed in the black box represent the experimental conditions used to validate the microkinetic model ((a), (b), (d) & (e)), and panels enclosed in the blue box represent the predictions using the developed model ((c) & (f)).

experiments, it also results in the small size of crystals. In literature, the smallest size of COF-5 crystal is reported to be 12 nm.[28,43] Since organic crystals smaller than 12 nm have not been observed in any of the spectroscopic or microscopic studies reported in the literature, it can be said that the crystals smaller than 12 nm are energetically unstable. The high surface-to-volume ratio results in high surface energy and increases the reactivity of such crystals. Beyond this size, lattice mismatch and low surface energy of the crystals reduce the reactivity of the crystals. The formation of COF-5 requires energetically stable nuclei with at least 750 SBU_1. The incubation time shown in all the panels of Fig. 3 is the time required to cross that nucleation window. The nucleation window is the set of reactions involving two or more clusters smaller than the energetically stable size (active crystals) to form a crystal of size equal to or greater than energetically stable size (inactive crystals). The dynamics of nucleation pathway while forming the smallest energetically stable crystal size are shown in Fig. S11,† and the details of the calculation are given in section S7 of the ESI.† The time represented on the *x*-axis about the peak in the dashed line, shown in all the panels of Fig. 3, is the time at which the rate of formation of inactive crystals is the highest. As the reaction proceeds, the crystalline fraction is dominated by inactive crystals. The relative rate of oriented attachment resulting in the formation of active crystals (step-growth) and inactive crystals (termination phase) start increasing after the concentration of active and inactive crystals is higher than SBU_1. Hence, the relative rate contribution of step and termination growth is lower and mostly seen at higher times. Similar results for phenol and formic acid catalysts are shown in Fig. S12 of the ESI.†

The effect of oriented attachment and the resulting grain size of COF-5 crystals using the theoretical microkinetic model (solid black line in Fig. 4a–f) and *ex situ* XRD (red scatter points in Fig. 4a–f), the subsequent evolution of water in the system, and the steady-state grain size distributions is shown in Fig. 4. The details of characterization using XRD and calculation of experimental grain size are given in section S8, and the standard deviation of the grain size from XRD is given in Table S5 of the ESI.† The parameters required to obtain results from the theoretical model are error minimized using the experimental results depicted in Fig. 4a, b, d, and e. Theoretical results shown in Fig. 4c and f are predicted using the optimized parameters. In Fig. 4a–f, the volumetric rates are shown in the background, where the blue region represents the destruction of higher-order crystals due to hydrolysis, the green region shows the volumetric rate of monomer addition, volumetric rate of oriented attachment resulting in active crystals is shown by orange region, and the volumetric rate of oriented attachment resulting into inactive crystals is shown by red region. The volumetric rates are plotted on the log–log scale to distinguish between the volumetric rates of different phases. After the formation of crystals higher than SBU_1, the

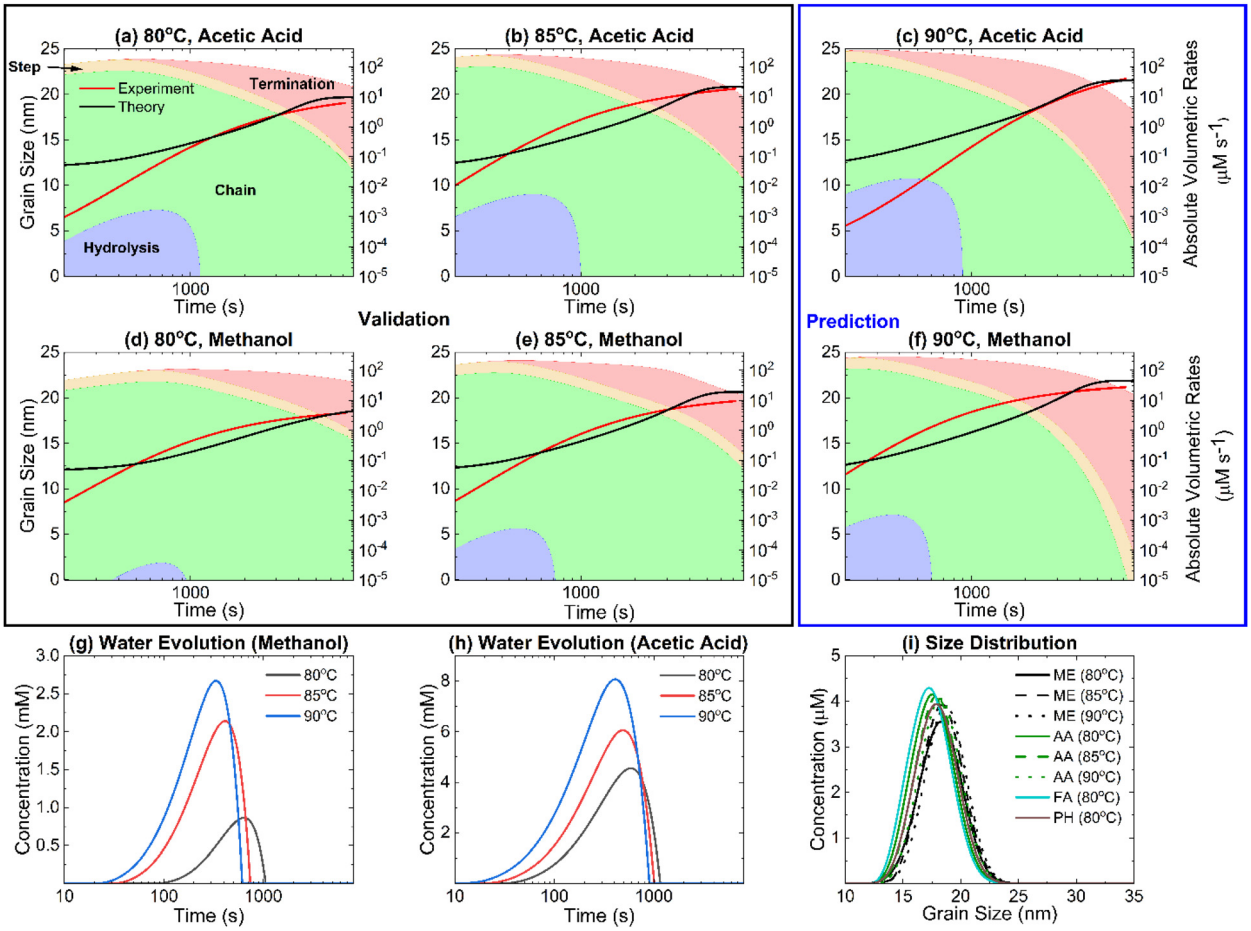

Fig. 4 The evolution of grain size of COF-5, formation of water in the solution as a function of temperature and catalyst, and the steady-state size distributions. The solid red line in panels (a)–(f) is obtained using the *ex situ* XRD technique. The solid black line in panels (a)–(f) is the grain size obtained from the theoretical microkinetic approach. The grain size is represented on the left *y*-axis. The background in panels (a)–(f) represents the volumetric rates of hydrolysis reaction (blue), chain addition (green), step-growth (orange), and termination phase (red). The volumetric rates are represented on the right *y*-axis. The titles of panels (a)–(f) represent the temperature and the catalyst used in the experiments. (a) 80 °C, acetic acid, (b) 85 °C, acetic acid, (c) 90 °C, acetic acid, (d) 80 °C, methanol, (e) 85 °C, methanol, (f) 90 °C, methanol, (g) water evolution in experiments with an acetic acid catalyst, (h) water evolution in experiments with methanol catalyst, (i) steady-state size distributions. Legend and terminologies defined in panel (a) apply to panels (a)–(f). In panel (i), the abbreviation ME refers to methanol, PH refers to phenol, FA refers to formic acid, and AA refers to acetic acid catalyst. Panels enclosed in the black box represent the experimental conditions used to validate the microkinetic model ((a), (b), (d) & (e)), and panels enclosed in the blue box represent the predictions using the developed model ((c) & (f)).

volumetric rate of oriented attachment always has a dominant contribution to the increase in grain size. Initially, the rate of oriented attachment resulting in active crystals is higher than the rate of oriented attachment resulting in inactive crystals. At higher times, the volumetric rate of formation of inactive crystals is exponentially higher than the volumetric rate of monomer addition and formation of active crystals. Similar results for phenol and formic acid catalysts are shown in Fig. S13 of the ESI.†

One of the significant results obtained from the theoretical model is that it yields mechanistic insight into the dynamics of grain size. The acetic acid catalyst yields a higher proton concentration in the solution than methanol, and hence the grain size observed in acetic acid catalyst experiments should be higher than the grain size observed in methanol catalysts experiments. Indeed, the steady-state grain size is higher for experiments with the acetic acid catalyst at all temperatures. However, the difference (around 2–4 nm depending on temperature) between the grain size is not significant compared to the exponential difference in the concentration of proton in the solution (see Fig. S14 in the ESI†). The insignificant difference can be attributed to the hydrolysis of larger crystals to form smaller crystals. For every formation of SBU_1 on the surface of crystals, two molecules of water are released. At low times, the concentration of water is not significant for both catalysts, and hence the grain size at initial times is not significantly different for the two catalysts. As the crystals involved in the oriented attachment increase, the water molecules are released proportionally. The increase in the concentration of water increases the volumetric rate of hydrolysis. The volu-

metric rate of hydrolysis results in a high concentration of SBU_1 in the system, and SBU_1 eventually breaks down into reactants pushing the system into the initiation phase. The competition between oriented attachment to form active and inactive crystals and the reversibility of the reaction due to water is the reason behind the insignificant difference between the grain size obtained using two different catalysts. Fig. 4g and h show the absolute concentration of water evolved during the formation of COF-5 as a function of temperature in the presence of acetic acid and methanol, respectively. The steady state grain size as a function of the water concentration at these experimental conditions is shown in Fig. S15 of the

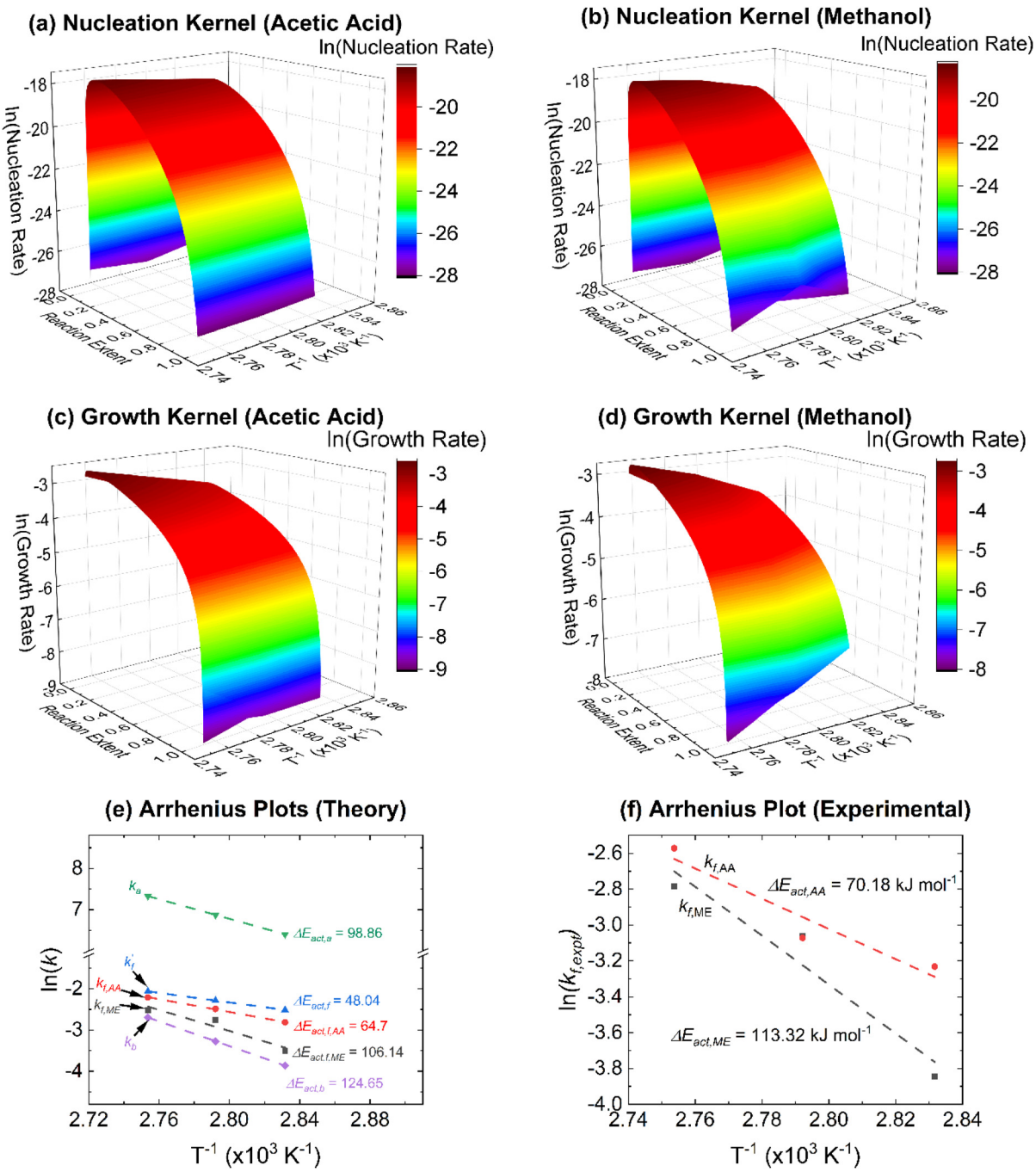

Fig. 5 Nucleation and growth kernels as a function of temperature and catalyst, and the Arrhenius plots. (a) Nucleation kernel for experiments with the acetic acid catalyst, (b) nucleation kernel for experiments with the methanol catalyst, (c) growth kernel for experiments with the acetic acid catalyst, (d) growth kernel for experiments with the methanol catalyst, (e) Arrhenius plots of the rate constants obtained by theoretical approach, and (f) Arrhenius plots of the rate constants obtained by fitting experimental data to integrated rate law. In panels (e) and (f), the abbreviation ME refers to methanol catalyst, and the abbreviation AA refers to acetic acid catalyst.

ESI.† Fig. 4i shows the steady-state size distribution of COF-5 as a function of temperature and catalyst. The mean of steady-state size distribution in experiments with a methanol catalyst is lower than the mean of steady-state size distribution in experiments with an acetic acid catalyst.

The information derived from the microkinetic model, which can be used to design and control the synthesis of COF-5, is presented in Fig. 5. Fig. 5a–d show the nucleation and growth kernels for the two different catalysts. The estimated nucleation and growth kernels are given in section S9 of the ESI.† The nucleation rate and growth rate depend upon two phases in the system: product and reactant. The fitting parameters with respect to the product phase (A_n) and (A_g) are very small, and the fitting parameters with respect to the reactant phase (B_n) and (B_g) are high, indicating that nucleation and growth rates depend highly upon the reactants. It can also be said that a higher initial concentration of the reactants would yield higher nucleation and growth rates. The activation barriers for nucleation and growth of COF-5 crystals in experiments with acetic acid as the catalyst are 25.12 and 81.27 kJ mol^{-1}, respectively. However, the activation barriers for nucleation and growth in experiments with methanol as the catalyst are 93.12 and 91.2 kJ mol^{-1}, respectively. The similar activation barriers for nucleation and growth of COF-5 crystals in the case of methanol catalyst indicate that there is no significant difference in the mechanism of nucleation and growth. It further validates that the low buffering capacity of methanol results in a slower rate of initiation reaction, thus preventing oriented attachment of COF-5 during nucleation and growth. The initial increase seen in the nucleation and growth kernels is because, initially, the rate is determined by the increase in the concentration of active crystals. The gradual decrease at a higher reaction extent is due to a higher concentration of inactive crystals in the system. Fig. 5e shows the Arrhenius plots for various rate constants involved in the formation of COF-5. At least one data point in each of the Arrhenius curves in Fig. 5b represents a predicted value. Fig. 5f shows the Arrhenius plots for the rate constants obtained by fitting experimental data to integrated rate law (see section S10 of the ESI†). The integrated rate law assumes a second-order reaction. The activation barrier for the SBU_1 formation reaction using integrated rate law is 70.18 and 113.32 kJ mol^{-1} for acetic and methanol catalysts, respectively. The activation barriers obtained by the theoretical model for SBU_1 formation for acetic acid and methanol catalysts are 64.65 kJ mol^{-1} and 106.14 kJ mol^{-1}, respectively. The activation energy obtained from the fitting of the limiting rate constant from the theoretical rate model is obtained as 48.04 kJ mol^{-1}. The difference between the lowest possible activation energy obtained from the theoretical approach and the activation energy calculated from experiments indicates that operating conditions can be modified to have higher proton concentration in the solution and achieve a faster synthesis of COF-5. Since the activation energy of the theoretical and experimental approaches match closely, it validates the mechanism of the SBU_1 formation reaction of COF-5. A summary of activation barriers and the pre-exponential factors obtained from Fig. 5e and f are given in Table S7 of the ESI.†

Conclusion

This work uncovers the kinetic moieties that are responsible for the formation of microcrystalline COF-5. Table S8 in the ESI† summarizes the governing molecular events that are responsible for each growth phase in COF-5 crystallization and polymerization. Along with an alternate proposed reaction pathway, the microkinetic model developed not only provides novel insights but also yields a quantitative foundation to the previously published hypothesis on COF-5 growth (see Tables S9 and S10 of the ESI†).

Enhanced initiation rates due to acid-catalyzed esterification, followed by oriented attachment and dissolution, govern the yield and grain size of COF-5 crystals, respectively. The relative rate contributions of various phases involved in the synthesis of COF-5 formation confirm that the crystalline yield of COF-5 depends significantly on the formation of SBUs.[14] The formation of SBUs is in turn governed by the proton concentration in the solution. The higher buffering capacity and higher concentration of protons given by acetic acid than methanol allow the transition of COF synthesis from the initiation and monomer addition phase to the oriented attachment phase. The resultant BET surface area based on the N_2 adsorption isotherm of the COF-5 crystals synthesized in this study is presented in Fig. S16 of the ESI.† To ensure that negligible amorphous proportions of COFs are obtained during the synthesis, TGA analysis were conducted on samples collected at different time stamps to ensure the crystalline nature of the obtained product (see Fig. S17†).

The higher-order SBUs formed due to SBU_1 dictate the grain size. The contribution of volumetric growth towards grain size due to oriented attachment is exponentially higher than monomer addition. The formation of larger grain size is further impeded by the release of water during oriented attachment. The lower pK_a of acetic acid allows the reaction to proceed to the larger size of crystals but, in turn, releases more water than the methanol catalyst and results in the dissolution of COF-5 crystals. The competitive effect of oriented attachment and release of water is the primary reason for the similar grain sizes obtained using both catalysts.

The nucleation and growth kernel yield direct insight into the difference in the yield and grain size of COF-5 observed in the presence of the two catalysts. The activation barriers for nucleation and growth of COF-5 crystals are higher in the case of methanol than acetic acid. Such quantitative data is critical to further optimize the batch and continuous synthesis strategies to fabricate thin films, adsorption beds, *etc.*, of crystalline COF-5 for a wide range of applications. Gas separations and catalysis applications have significant dependence on the domain size, porosity, and surface areas of the polymeric network. Manipulation of these processing variables effectively controls these aspects of COF-5, as shown in this work.

Although the results in this article are presented only for COF-5, the inexpensive experimental approach and the simplicity of the microkinetic model allow the extension of this approach to a wide range of 2D and 3D COFs.

Conflicts of interest

The authors declare that there are no competing interests.

Acknowledgements

This material is based on the work performed at the Materials and Systems Engineering Laboratory at the University of Illinois Chicago (UIC). M. R. S. acknowledges funding support from UIC and the US National Science Foundation (NSF, EFRI 2132022). We thank Laboratory Computing Resources Center (LCRC) of Argonne National Laboratory for providing computational resources to perform theoretical calculations. This work made use of the Nanotechnology Core Facility (NCF) facilities at UIC for XRD measurements. This work also made use of the EPIC facility of Northwestern University's NUANCE Center for SEM measurements, which has received support from the SHyNE Resource (NSF ECCS-2025633), the IIN, and Northwestern's MRSEC program (NSF DMR-1720139). The authors would like to acknowledge Neil Schweitzer (REACT facilities) at Northwestern University for assisting with BET measurements. This work made use of the IMSERC at Northwestern University, which has received support from the NSF (CHE-1048773 and DMR0521267).

References

1 A. J. Rieth, A. M. Wright and M. Dinca, Kinetic stability of metal-organic frameworks for corrosive and coordinating gas capture, *Nat. Rev. Mater.*, 2019, **4**, 708–725.
2 J. Guo and D. Jiang, Covalent Organic Frameworks for Heterogeneous Catalysis: Principle, Current Status, and Challenges, *ACS Cent. Sci.*, 2020, **6**, 869–879.
3 J. Ozdemir, *et al.*, Covalent Organic Frameworks for the Capture, Fixation, or Reduction of CO2, *Front. Energy Res.*, 2019, **7**(77).
4 R. K. Sharma, *et al.*, Recent development of covalent organic frameworks (COFs): synthesis and catalytic (organic-electro-photo) applications, *Mater. Horiz.*, 2020, **7**, 411–454.
5 F. Yu, *et al.*, Electrochromic two-dimensional covalent organic framework with a reversible dark-to-transparent switch, *Nat. Commun.*, 2020, **11**, 5534.
6 J. Li, *et al.*, Bulk COFs and COF nanosheets for electrochemical energy storage and conversion, *Chem. Soc. Rev.*, 2020, **49**, 3565–3604.
7 K. Geng, *et al.*, Covalent Organic Frameworks: Design, Synthesis, and Functions, *Chem. Rev.*, 2020, **120**, 8814–8933.
8 M. J. Kalmutzki, N. Hanikel and O. M. Yaghi, Secondary building units as the turning point in the development of the reticular chemistry of MOFs, *Sci. Adv.*, 2018, **4**, eaat9180.
9 M. S. Lohse and T. Bein, Covalent Organic Frameworks: Structures, Synthesis, and Applications, *Adv. Funct. Mater.*, 2018, **28**, 1705553.
10 S. Kandambeth, *et al.*, Construction of crystalline 2D covalent organic frameworks with remarkable chemical (acid/base) stability via a combined reversible and irreversible route, *J. Am. Chem. Soc.*, 2012, **134**, 19524–19527.
11 Y. Jia, *et al.*, 8-Hydroxyquinoline functionalized covalent organic framework as a pH sensitive carrier for drug delivery, *Mater. Sci. Eng., C*, 2020, **117**, 111243.
12 S. A. Ahmed, *et al.*, pH-Dependent Slipping and Exfoliation of Layered Covalent Organic Framework, *Chemistry*, 2020, **26**, 12996–13001.
13 H. J. Zhu, *et al.*, Efficient electron transmission in covalent organic framework nanosheets for highly active electrocatalytic carbon dioxide reduction, *Nat. Commun.*, 2020, **11**, 497.
14 H. Li, *et al.*, Nucleation and Growth of Covalent Organic Frameworks from Solution: The Example of COF-5, *J. Am. Chem. Soc.*, 2017, **139**, 16310–16318.
15 I. Castano, *et al.*, Chemical Control over Nucleation and Anisotropic Growth of Two-Dimensional Covalent Organic Frameworks, *ACS Cent. Sci.*, 2019, **5**, 1892–1899.
16 B. T. Koo, R. F. Heden and P. Clancy, Nucleation and growth of 2D covalent organic frameworks: polymerization and crystallization of COF monomers, *Phys. Chem. Chem. Phys.*, 2017, **19**, 9745–9754.
17 T. Ma, *et al.*, Diverse crystal size effects in covalent organic frameworks, *Nat. Commun.*, 2020, **11**, 6128.
18 T. Sick, *et al.*, Oriented Films of Conjugated 2D Covalent Organic Frameworks as Photocathodes for Water Splitting, *J. Am. Chem. Soc.*, 2018, **140**, 2085–2092.
19 K. Dey, S. Bhunia, H. S. Sasmal, C. M. Reddy and R. Banerjee, Self-Assembly-Driven Nanomechanics in Porous Covalent Organic Framework Thin Films, *J. Am. Chem. Soc.*, 2021, **143**, 955–963.
20 R. L. Li, *et al.*, Controlled growth of imine-linked two-dimensional covalent organic framework nanoparticles, *Chem. Sci.*, 2019, **10**, 3796–3801.
21 S. Bi, *et al.*, Two-dimensional semiconducting covalent organic frameworks via condensation at arylmethyl carbon atoms, *Nat. Commun.*, 2019, **10**, 2467.
22 V. Lakshmi, *et al.*, A Two-Dimensional Poly(azatriangulene) Covalent Organic Framework with Semiconducting and Paramagnetic States, *J. Am. Chem. Soc.*, 2020, **142**, 2155–2160.
23 R. van der Jagt, *et al.*, Synthesis and Structure-Property Relationships of Polyimide Covalent Organic Frameworks for Carbon Dioxide Capture and (Aqueous) Sodium-Ion Batteries, *Chem. Mater.*, 2021, **33**, 818–833.
24 H. Fan, *et al.*, MOF-in-COF molecular sieving membrane for selective hydrogen separation, *Nat. Commun.*, 2021, **12**, 38.

25 X. L. Li, *et al.*, Expeditious synthesis of covalent organic frameworks: a review, *J. Mater. Chem. A*, 2020, **8**, 16045–16060.
26 X. Chen, *et al.*, Designed synthesis of double-stage two-dimensional covalent organic frameworks, *Sci. Rep.*, 2015, **5**, 14650.
27 S. Dalapati, *et al.*, Rational design of crystalline supermicroporous covalent organic frameworks with triangular topologies, *Nat. Commun.*, 2015, **6**, 7786.
28 B. J. Smith, *et al.*, Colloidal Covalent Organic Frameworks, *ACS Cent. Sci.*, 2017, **3**, 58–65.
29 H. Li, *et al.*, Synthesis of covalent organic frameworks via in situ salen skeleton formation for catalytic applications, *J. Mater. Chem. A*, 2019, **7**, 5482–5492.
30 L. Wang, *et al.*, A highly soluble, crystalline covalent organic framework compatible with device implementation, *Chem. Sci.*, 2019, **10**, 1023–1028.
31 R. A. Maia, *et al.*, Small-angle X-ray scattering as a multifaceted tool for structural characterization of covalent organic frameworks, *J. Appl. Crystallogr.*, 2020, **53**, 1376–1386.
32 C. S. Tsao, *et al.*, Characterization of pore structure in metal-organic framework by small-angle X-ray scattering, *J. Am. Chem. Soc.*, 2007, **129**, 15997–16004.
33 B. J. Smith, N. Hwang, A. D. Chavez, J. L. Novotney and W. R. Dichtel, Growth rates and water stability of 2D boronate ester covalent organic frameworks, *Chem. Commun.*, 2015, **51**, 7532–7535.
34 B. J. Smith, A. C. Overholts, N. Hwang and W. R. Dichtel, Insight into the crystallization of amorphous imine-linked polymer networks to 2D covalent organic frameworks, *Chem. Commun.*, 2016, **52**, 3690–3693.
35 B. J. Smith and W. R. Dichtel, Mechanistic studies of two-dimensional covalent organic frameworks rapidly polymerized from initially homogenous conditions, *J. Am. Chem. Soc.*, 2014, **136**, 8783–8789.
36 A. M. Evans, *et al.*, Seeded growth of single-crystal two-dimensional covalent organic frameworks, *Science*, 2018, **361**, 52–57.
37 R. R. Bhawnani, *et al.*, Percolation-assisted coating of metal-organic frameworks on porous substrates, *J. Membr. Sci.*, 2023, **668**, 121202.
38 A. V. Dighe, R. Y. Nemade and M. R. Singh, Modeling and Simulation of Crystallization of Metal–Organic Frameworks, *Processes*, 2019, **7**, 11.
39 A. P. Cote, *et al.*, Porous, crystalline, covalent organic frameworks, *Science*, 2005, **310**, 1166–1170.
40 H. R. Abuzeid, A. F. El-Mahdy and S.-W. Kuo, Covalent organic frameworks: Design principles, synthetic strategies, and diverse applications, *Giant*, 2021, **6**, 100054.
41 A. V. Bandura and S. N. Lvov, The Ionization Constant of Water over Wide Ranges of Temperature and Density, *J. Phys. Chem. Ref. Data*, 2006, **35**, 15–30.
42 A. V. Dighe, *et al.*, Autocatalysis and Oriented Attachment Direct the Synthesis of a Metal-Organic Framework, *JACS Au*, 2022, **2**, 453–462.
43 D. D. Medina, *et al.*, Room Temperature Synthesis of Covalent–Organic Framework Films through Vapor-Assisted Conversion, *J. Am. Chem. Soc.*, 2015, **137**, 1016–1019.